Hindawi

Research Article

Design and Analysis of a Multiple and Wide Nulling Collaborative Beamforming Scheme in the Domain of 3-Dimensional Wireless Sensor Networks

Robert Macharia Maina [1], Philip Kibet Langat,[2] and Peter Kamita Kihato[3]

[1]*Department of Electrical and Electronic Engineering, Pan African University Institute for Basic Sciences, Technology and Innovation, Nairobi, Kenya*
[2]*Department of Telecommunication and Information Engineering, Jomo Kenyatta University of Agriculture and Technology, Nairobi, Kenya*
[3]*Department of Electrical and Electronic Engineering, Jomo Kenyatta University of Agriculture and Technology, Nairobi, Kenya*

Correspondence should be addressed to Robert Macharia Maina; robertisaacm@gmail.com

Null steering is essential in collaborative beamforming (CB) in wireless sensor networks (WSNs) to ensure minimal radiation power and interference in the direction of unintended receivers. Current research in null steering in CB in WSNs is mainly from the perspective of planar arrangements of sensor nodes and sink(s). Furthermore, there is no research dedicated to the formation of multiple wide nulls during CB in 3-dimension WSNs. Wide nulls are ideal in scenarios featuring mobile unintended sink(s). A new multiple and wide null steering scheme applicable to CB in WSNs is presented in this work (from the perspective of a 3-dimensional random arrangement of static sensor nodes). It is assumed that desired nulling directions are implicitly known at a CB cluster head. A particle swarm optimization (PSO) algorithm variant is applied in concurrent node transmit amplitude and phase perturbation with an aim of achieving beam steering alongside multiple and wide null steering. The performance of the proposed null steering scheme is validated against a basic null steering approach (with reference to current literature). Furthermore, a comparative null depth, width, and nulling accuracy analysis are done upon varying the count of collaborating nodes and the collaborating cluster radius. An increase in the number of collaborating nodes is found to increase nulling depth at an exponentially decaying rate. An increase in the collaborating nodes' cluster radius yields a reduction in null width. The contributions of this work to the existing literature are as follows: (i) the design and investigation of a null steering scheme from the perspective of a 3-dimension random arrangement of sensor nodes; (ii) the design of a concurrent beam steering and multiple wide null steering scheme on the basis of concurrent node transmit amplitude and phase perturbation whilst ensuring null depth uniformity; (iii) a statistical analysis of the impact of a count of collaborating nodes and collaborating cluster radius on nulling performance; (iv) investigation of capacity improvement at unintended receivers upon null steering.

1. Introduction

Collaborative beamforming (CB) is a useful tool for establishing energy-efficient and reliable communication links between wireless sensor network (WSN) nodes and far-off sinks [1–3]. CB in WSNs is vital given that sensor nodes are usually energy-limited and sinks are usually located beyond individual nodes' transmission range. CB serves to overcome the shortcomings associated with multihop transmission in WSNs such as the dependency of transmission quality on individual sensors, high communication overheads, delay, and increased network interference [4]. CB is achieved through appropriate transmit amplitude and phase weighting at a carefully selected set of nodes with an aim of ensuring a constructive combination of individual node radiation

energy in the sink's direction. Collaborating nodes more or less form a virtual random antenna array.

CB is often associated with high sidelobes owing to the usual random placement of collaborating nodes [5–7]. The high sidelobes are bound to yield interference at unintended cochannel terminals. Minimizing CB radiation in unintended receiver(s)' direction(s) is of utmost necessity. In centralized antenna arrays, null-steering beamformers have been applied to yield a destructive combination of radiation in the undesired direction(s) while ensuring a constructive combination of radiation in the desired direction(s) [8–12]. Metaheuristic optimization algorithms are essential towards this end. A typical application of a metaheuristic optimization algorithm can be found in [13].

1.1. Related Work. In [8], an adaptive null steering beamformer is designed on the basis of a uniform linear array (ULA). The bat algorithm (BA) is utilized in the designed beamformer to optimally adjust transmit amplitude at each array element. The resultant null steering performance has been analyzed against approaches utilizing accelerated particle swarm optimization (APSO) and genetic algorithm (GA). The BA-driven beamformer is noted to outperform the APSO and GA-driven beamformers in terms of null steering precision, null breadth, and convergence speed. The essence of deep and broad nulls alongside effective optimizing algorithms is clearly brought to the fore. In [9], a triple-mode circular microstrip patch antenna bearing the capability of forming two nulls within a select hemisphere is presented. Furthermore, the two nulls can be steered independently. The designed antenna consists of

  (i) A central circular patch supporting TM11 mode

  (ii) A TM21 mode shorted annular ring around the central circular patch

  (iii) A shorted annular ring supporting TM31 mode encircling the other two radiators

The three modes (TM11, TM21, and TM31) are fed using two feed points with an aim of creating right-handed circular polarization. The resultant radiation pattern is manipulated to yield two independently steerable nulls through apt control of individual feed amplitude and phase. A hybrid particle swarm optimization (PSO) and pattern search algorithm are applied in feed amplitude and phase optimization. A beamforming network consisting of digital variable gain attenuators, digital phase shifters, and low-noise amplifiers is utilized in the optimal feed amplitude and phase implementation process. The designed beamformer bears limited main beam steering. The research brings to the fore the practical aspects of null steering implementation. In [10], an improved invasive weed optimization (IWO) algorithm is applied in concurrent multiple beamforming and null steering. The improved IWO algorithm is utilized in optimizing the excitation amplitude at a linear time-modulated antenna array elements to yield optimal beams and nulls. In [11], a coherently radiating periodic structure (CORPS) beamforming network with beam and null steering capability is proposed. The PSO algorithm is applied in

optimizing excitation weights in the CORPS beamforming network to generate an array factor bearing desired sidelobe level, directivity, and null depth. In [12], a combined minimum variance distortionless response (MVDR) and firefly algorithm (FA) approach is utilized in null steering in a linear antenna array. Deep and accurate nulls are obtained. In [14], an array of four patch antennas in conjunction with a set of eight phase shifters is utilized to synthesize steerable nulls. In [15], a distributed beamforming network made up of multiple dual transmitters is investigated in terms of beam and null steering. A groupwise null forming scheme is proposed. Numerical simulations validate the effectiveness of the proposed scheme. The authors in [16] a set of novel beamforming schemes for synthetic aperture radar are presented. A notable outcome is a trough-like beam pattern with wide nulls. Consequently, interference signals received by synthetic aperture radar can be suppressed effectively. Numerical simulations alongside experimental results validate the effectiveness of the proposed schemes. Null steering is investigated in the planar ring; uniformly distributed and volumetric shell antenna element distributions are shown in reference [17]. In [18], a null steering scheme based on the partitioning of a Mobile ad hoc Network (MANET) node into a set of 2 subarrays is presented. The authors in [19] present a novel heuristic optimization algorithm christened Fibonacci branch search (FBS). The algorithm is applied in the design of a low sidelobe and deep nulling adaptive beamformer.

As per the reviews done, research in null steering in conventional (stand-alone) antenna array beamformers is mainly on the basis of uniform array geometry (particularly linear configuration). On the other hand, WSN nodes are usually randomly arranged. In stand-alone antenna array beamforming, there is complete and accurate knowledge of antenna element positioning (geometry) unlike in CB in WSNs.

The null-steering concept has been extended to CB in WSNs in [20, 21]. Application of null-steering is bound to increase Signal to interference and noise ratio (SINR) at the unintended receivers and potentially enhance network security against intercepting terminals.

In [20], a fully distributed nulling steering procedure is proposed in the domain of an Internet of Things (IoT) network (bearing a decentralized architecture). Herein, nulling steering is applied to enhance secrecy performance. This is particularly important when an eavesdropper is located in a high sidelobe region of a CB outcome. It is shown that there exists an optimal degree of nulling that maximizes the secrecy performance. In [21], a node selection-based mechanism (in the sense of yielding a virtual linear array) is utilized in null steering.

Other recent studies pertaining to CB in WSNs (although without nulling considerations) can be found in [22–27].

In [27], research entailing simultaneous optimization of beamforming, power consumption, and energy harvesting schemes in a WSN is carried out. The applied beamforming concept entails the use of multiple antennas at base stations, resulting in optimal signal and energy transmission toward

intended sinks. The transmitted signals encompass data and energy that ought to be sent to mobile nodes. The nodes are expected to split received power into data and energy (energy harvesting). Although the presented research is to a great extent different from the null steering research presented in this paper, the authors highlight the significance of power saving at WSN nodes (in particular extending node lifetime).

General studies entailing the application of metaheuristic optimization algorithms in WSNs can be found in [28–33]. Recent artificial intelligence applications (not limited to WSNs) can be found in [34–36].

In [6] capacity improvement analysis at unintended receivers (accrued from sidelobe reduction in CB) is analyzed. In the paper, an average reduction of 20 dB in peak sidelobe level and 162 percent capacity improvement is reported in the worst case scenario.

1.2. Literature Review Summary. Observations made in current null steering research (in the context of CB in WSNs) are as per the following listing:

(1) Multiple unintended sink(s) in 3-dimension WSN configuration have not been considered

(2) There is no research on the formation of wide nulls (ideal in scenarios featuring mobile unintended sink(s))

The contributions brought forward in this paper include

(1) Formulation of a wide multiple nulling scheme from the perspective of a 3-dimension WSN using an appropriate metaheuristic optimization algorithm

(2) Analysis of capacity performance at unintended receivers upon nulling

(3) Nulling performance analysis with changes in CB cluster radius and number of collaborating nodes

Utilized performance measures include nulling depth, width, and accuracy.

Practical applications of the outcomes presented in this manuscript would be in

(i) Environmental monitoring problems as addressed in [37, 38]

(ii) Traffic control in cities [39]

(iii) Industrial monitoring/control [40]

(iv) "Smart" cities [41, 42]

(v) Health monitoring [43]

(vi) "Smart" home applications [44]

(vii) "Smart" agriculture applications [45, 46]

The rest of the paper is organized as follows: Section 2 presents the methodology. The sections presented in the methodology include the development of a 3-dimension CB model and the development of a multiple and wide nulling scheme, alongside the general simulation setup. The obtained results are presented and discussed in Section 3. The overall concluding remarks are presented in Section 4.

2. Methodology

2.1. 3-Dimension CB Model. Figure 1 illustrates a 3-dimensional random distribution of WSN nodes.

The considered model encompasses a large variety of practical WSN deployment scenarios wherein sensor nodes are randomly distributed in a 3-dimensional manner. The considerations made in the model design process are as per the following list:

(1) 3-dimension sensor node and sink distribution.

(2) A node is selected from a set of collaborating nodes to act as a cluster head/CB coordinator. The cluster head also serves as the reference point in mapping out the other collaborating nodes' geometric positions: the nodes are taken as situated at a distance r, azimuth angle ψ, and elevation angle ϑ) with reference to the cluster head.

(3) With reference to the cluster head location, the sink is located at an elevated location (A, ϕ, θ).

(4) All nodes are synchronized in phase and frequency. As such, this condition is difficult to meet in practice unless high-precision clocks are utilized in the collaborating nodes.

(5) All nodes are location-aware.

(6) The nodes are equipped with identical isotropic antennas.

(7) There is negligible mutual coupling between nodes.

(8) Path loss is identical between the sink and all nodes participating in the CB process.

(9) The nodes and sinks are static during the CB process.

(10) There is a perfect time-invariant channel between the sink and nodes participating in the CB process.

Figure 2 depicts a typical far-field radiation problem. In subsequent expressions and with reference to Figure 2,

(i) Angle $P'OQ$ is symbolized as ψ

(ii) **r** is the position vector of the far-field observation point

(iii) **r**$'$ is the position vector of the radiator

The magnetic potential at the far-field observation point as a consequence of the radiator current density is as per the following equation [47]:

$$A(r,t) = \int_v \frac{\mu J(r', t - R/C)}{4\pi R} d^3 r',\qquad(1)$$

where

(i) $\int_v$ is representative of the volume integral about the immediate region surrounding the radiator

(ii) μ: permeability constant

(iii) **J** is the radiator current density

(iv) t: observation time

(v) C: wave velocity
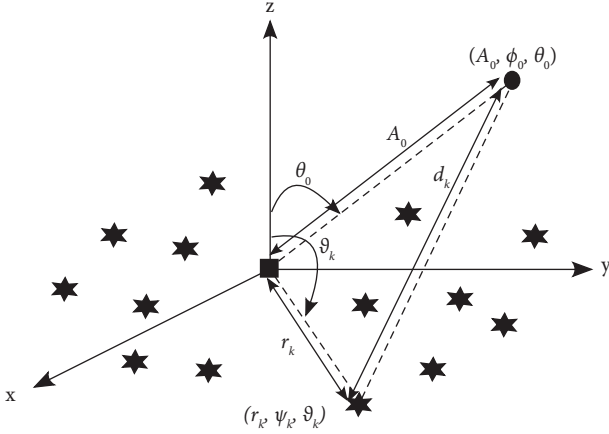
(vi) d: radiator dimension

FIGURE 1: Wireless sensor network model (a 3-dimensional perspective from the point of view of both node distribution and sink location). Cluster head: rectangular symbol; sensor nodes: star symbol; sink: circular symbol.
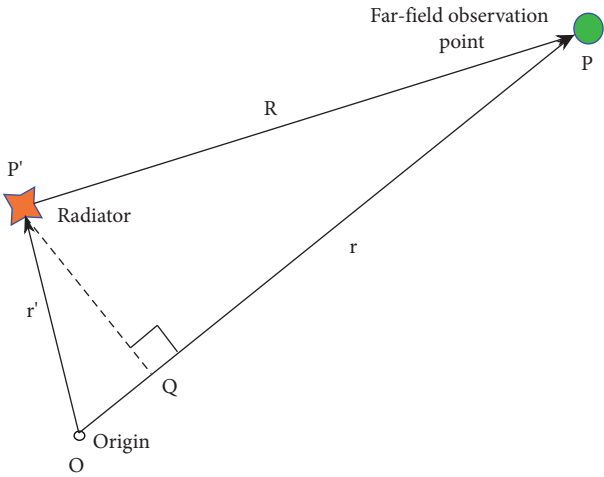

FIGURE 2: Far-field radiation problem.

Considering a single-frequency wave, equation (1) takes the form of the following equation:

$$A(\mathbf{r})e^{jwt} = \int_{v} \frac{\mu \mathbf{J}(\mathbf{r})e^{jw(t-R/C)}}{4\pi R}d^3\mathbf{r}'. \tag{2}$$

Equation (2) can be written as follows:

$$A(\mathbf{r}) = \int_{v} \frac{\mu \mathbf{J}(\mathbf{r}')e^{-jkR}}{4\pi R}d^3\mathbf{r}', \tag{3}$$

where $k = \omega/C = 2\pi/\lambda$.

As per Figure 2, the dimensions PP' and PQ of the triangle PQP' are approximately equal (considering far distances). $PQ = OP - OQ$. The distance R can be expressed as follows:

$$R \approx r - \widehat{\mathbf{r}}.\mathbf{r}' = r - r'\cos(\psi). \tag{4}$$

Using the approximation given in equation (4) in the exponential part of (3) and the approximation $R \approx r$ in the denominator yields

$$A(\mathbf{r}) = \int_{v} \frac{\mu \mathbf{J}(\mathbf{r}')e^{-jk\left(r-\widehat{\mathbf{r}}.\mathbf{r}'\right)}}{4\pi r}d^3\mathbf{r}'. \tag{5}$$

Equation (5) can be written as

$$A(\mathbf{r}) = \frac{\mu e^{-jkr}}{4\pi r}\int_{v} \mathbf{J}(\mathbf{r}')e^{j k\widehat{\mathbf{r}}.\mathbf{r}'}d^3\mathbf{r}'. \tag{6}$$

The integral factor (equation (7) radiation vector) in equation (6) determines the directional properties of the radiated field.

$$\mathbf{F}(\mathbf{k}) = \int_{v} \mathbf{J}(\mathbf{r}')e^{j\mathbf{k}.\mathbf{r}'}d^3\mathbf{r}', \tag{7}$$

where $\mathbf{k} = k\widehat{\mathbf{r}}$.

Given a three-dimension array of several identical antennas located at positions $[\mathbf{R}_0, \mathbf{R}_1, \mathbf{R}_2, \ldots \mathbf{R}_T]$, with relative feed current coefficients $[a_0, a_1, a_2, \ldots a_T]$, the current density corresponding to the tth antenna is as

$$\mathbf{J}_t(\mathbf{r}') = a_t \mathbf{J}(\mathbf{r} - \mathbf{R_t}). \tag{8}$$

The corresponding radiation vector is as

$$\mathbf{F}_t(\mathbf{k}) = a_t e^{j\mathbf{k}.\mathbf{R_t}}\mathbf{F}(\mathbf{k}). \tag{9}$$

The total radiation vector given T radiators is as follows, the respective array factor being $\sum_{t=0}^{T} a_t e^{j\mathbf{k}.\mathbf{R_t}}$.

$$\mathbf{F}_{tot}(\mathbf{k}) = \sum_{t=0}^{T}\left(a_t e^{j\mathbf{k}.\mathbf{R_t}}\right)\mathbf{F}(\mathbf{k}). \tag{10}$$

Given a set of T nodes featuring arbitrary placement/distribution, the array factor magnitude in the direction (ϕ, θ) may be expressed as

$$AF_{\phi,\theta} \approx \sum_{t=1}^{T} w_t e^{j2\pi/\lambda\left[\mathbf{R_t}.\widehat{\mathbf{r}}\right]}, \tag{11}$$

where

(i) $\mathbf{R}_t$: position vector of tth node. $\mathbf{R}_t = r_{tx}\mathbf{a}_x + r_{ty}\mathbf{a}_y + r_{tz}\mathbf{a}_z$

(ii) $\widehat{\mathbf{r}} = \sin(\theta)\cos(\phi)\mathbf{a}_x + \sin(\theta)\sin(\phi)\mathbf{a}_y + \cos(\theta)\mathbf{a}_z$

(iii) • is the dot product operator

Upon wavelength normalization, equations (11) can be expressed as

$$AF_{\phi,\theta} \approx \sum_{t=1}^{T} w_t e^{j2\pi\left[\widetilde{\mathbf{R}_t}.\widehat{\mathbf{r}}\right]}, \tag{12}$$

where $\widetilde{\mathbf{R}}_t = \mathbf{R}_t/\lambda$.

2.2. Proposed Null Steering Scheme. In the proposed CB scheme, null steering is done concurrently with beam steering. Wide and deep nulls are the intended outcome. Wide nulls are beneficial in the following two ways:

(i) Reduction of interference in other distinct CB clusters (collaborating nodes are bound to be spatially distributed)

(ii) Reduction of CB frequency in cases of slightly mobile unintended receivers

(iii) Let

(iv) (ϕ_0, θ_0) be the direction of the intended sink with reference to the cluster head.

(v) (ϕ_u, θ_u) be a substantial subset of all undesired radiation directions, where $u \in [1, 2 \ldots U]$.

(vi) (ϕ_n, θ_n) be the unintended sink direction(s) with reference to the cluster head, where $n \in [1, 2 \ldots N]$.

(vii) $\text{MAF}_{(\phi_n, \theta_n)}(\mathbf{W})$ be the mean AF in the immediate neighborhood of (ϕ_n, θ_n).

The objectives to be met are as per equations (13)–(16).

The objective function in equation (13) is geared towards beam steering (maximizing radiation in the intended sink direction).

$$\text{maximize:} \quad \left|AF_{\phi_0, \theta_0}(\mathbf{W})\right|^2. \tag{13}$$

The objective function in equation (14) ensures minimal radiation power spread in all directions outside of the intended sink direction.

$$\text{minimize:} \quad \frac{1}{U} \sum_{u=1}^{U} \left|AF_{\phi_u, \theta_u}(\mathbf{W})\right|^2. \tag{14}$$

The objective function in equation (15) is geared towards null steering (minimizing radiation in the unintended sink direction(s)).

$$\text{minimize:} \quad \frac{1}{N} \sum_{n=1}^{N} \left|AF_{\phi_n, \theta_n}(\mathbf{W})\right|^2. \tag{15}$$

The objective function in equation (16) specifically caters to wide nulls.

$$\text{minimize:} \quad \frac{1}{N} \sum_{n=1}^{N} \left|MAF_{(\phi_n, \theta_n)}(\mathbf{W})\right|^2. \tag{16}$$

The overall objective function to be optimized is a weighted (g_x) combination of the objectives given in equations (13)–(16) as per (17) where $\sum_{x=1}^{4} g_x = 1$. The weighting values (g_x) have been carefully selected to yield the best possible outcome. In particular, the values utilized for g_1, g_2, g_3 and g_4 are 03, 0.2, 0.3, and 0.2, respectively. The values so chosen accord beam steering and nulling comparatively higher weighting in comparison to generalized minimization of radiation in undesired directions and null widening. An exhaustive search entailing various sets of values for g_1, g_2, g_3 and g_4 yielded the afore-stated values as optimal in terms of overall CB solution quality.

$$\begin{aligned}
\text{minimize:} \quad f(\mathbf{W}) = &\left(-g_1 \left|\text{AF}_{\phi_0, \theta_0}(\mathbf{W})\right|^2 \right. \\
&\left. + g_2 \frac{1}{U} \sum_{u=1}^{U} \left|\text{AF}_{\phi_u, \theta_u}(\mathbf{W})\right|^2\right) \\
&+ \left(g_3 \frac{1}{N} \sum_{n=1}^{N} t_n \left|\text{AF}_{\phi_n, \theta_n}(\mathbf{W})\right|^2 \right. \\
&\left. + g_4 \frac{1}{N} \sum_{n=1}^{N} \left|\text{MAF}_{(\phi_n, \theta_n)}(\mathbf{W})\right|^2\right).
\end{aligned} \tag{17}$$

t_n is a weighting factor selected for every optimization iteration in accordance with the value of $\text{AF}_{\phi_n, \theta_n}$. This allows for a balanced nulling scheme wherein all null values are nearly identical. In particular, for a 3-null case, the utilized values of t_n are 0.5, 0.3, and 0.2 for descending values of $\text{AF}_{\phi_n, \theta_n}$.

A PSO algorithm variant (Culled-Fuzzy-Adaptive PSO (CFAPSO) algorithm [48]) has been utilized in optimizing (selecting the best possible node weights $\mathbf{W}$) the designed multiobjective function (equation (17)) The CFAPSO algorithm is described in Section 2.3.

2.3. Culled-Fuzzy-Adaptive PSO Algorithm. PSO algorithm entails a carefully checked movement of a swarm of "particles" (bearing potential solutions to a given problem) in a defined search space [49–51]. Equations (18) (velocity update equation) and (19) (position update equation) represent the basic PSO algorithm.

$$\begin{aligned}
v_i(t+1) = &\left(wv_i(t)\right) + \left(c_p r_p \left(p_i - x_i\right)\right) \\
&+ \left(c_s r_s \left(l_i - x_i\right)\right),
\end{aligned} \tag{18}$$

$$x_i(t+1) = x_i(t) + v_i(t+1). \tag{19}$$

In the velocity and position update equations above

(i) t represents iteration count.

(ii) i denotes a swarm particle.

(iii) x_i and v_i denote the position and velocity of particle i, respectively.

(iv) w denotes inertia weight. w controls the influence of the immediate previous velocity in the velocity update equation. In the basic PSO algorithm, w is decreased linearly from 0.9 in the first algorithm iteration to 0.4 in the last algorithm iteration [52].

(v) p_i represents the personal best position.

(vi) l_i represents the global best position.

(vii) c_p and c_s represent the personal/self and social confidence parameters, respectively. c_p and c_s control the influence of the personal and global best positions, respectively, in the velocity update equation. In the standard PSO algorithm, c_p and c_s are fixed at 2 [53].

(viii) r_p/r_s are random numbers within the range $[0 - 1]$. r_p and r_s enhance exploration capabilities of personal and social influences.

c_p and c_s have a fundamental influence on the PSO algorithm performance. c_p and c_s values ought to be judiciously chosen in line with the optimization problem under consideration. Large values of c_p relative to c_s heighten search space exploration. Large values of c_s relative to c_p heighten exploitation and convergence to a global solution. Consequently, it is ideal to have adaptive values of c_p and c_s rather than the static values distinctive of the basic PSO algorithm.

In the CFAPSO algorithm used in this manuscript, the values of c_p and c_s are mapped onto the range (2–2.4) and (2.2–2.6), respectively on the basis of iteration count and particle performance index [48]. w is mapped onto the range (0.4–0.9). The mapping process of c_p, c_s, and w is done using a fuzzy logic inference system.

In summary, the procedure followed in implementing the CFAPSO Algorithm 1 is as per the following steps:

2.4. Simulation Setup.

The research work laid out in this manuscript has been carried out through appropriate simulations in Matlab software. The Matlab environment offers a numeric computing platform suitable for beamforming strategies modeling, optimization, and analysis.

CB analysis entailing varying WSN node count and cluster radius has been carried out. The utilized WSN arrangements with node count variation are as per Figure 3 and Tables 1 and 2. The utilized WSN arrangements with cluster radius variation are as per Figure 4 and Table 3. All node distances are normalized with respect to wavelength.

In this research work, fifty independent tests have been used for every optimization procedure. This conforms to the requirement that sample sizes greater than 30 are by and large sufficient for a bulk of data distributions for the central limit theorem to hold [54]. The central limit theorem is crucial in statistical data analysis for two chief reasons [55].

(i) Precise data analysis estimates: sampling distributions of the mean cluster tightly around the population mean with increasing sample size.

(ii) Normality assumption: the fact that sampling distributions can approximate a normal (Gaussian) distribution is critical for use of parametric hypothesis tests of the mean.

In this manuscript, the statistical tools used in the results analysis process are as follows:

(1) Analysis of variance (ANOVA) test: a test aimed at testing whether or not two or more sample/population means are statistically identical [56]

(2) Tukey–Kramer test: a post hoc analysis test aimed at pin-pointing the exact sample/population means that have statistically significant differences [57]

Listed below are the general simulation considerations.

(i) 3 null steering directions

(ii) A single-beam steering direction

(iii) All node distances are wavelength-normalized

(iv) Sixty CFAPSO algorithm iterations are utilized for the CB optimization problems addressed

(v) A CFAPSO algorithm swarm size of thirty has been adopted

(vi) Beamforming outcomes have been presented qualitatively in the form of radiation power pattern plots and quantitatively in terms of null depth values, null width values, nulling accuracy, and radiation power in desired/undesired directions.

3. Results and Discussion

Herein, the performance of the developed null steering beamformer (as per equation (17)) is weighed against that of a basic null steering beamformer. The applied basic null steering beamformer does not take into consideration aspects of null width control, null depth fine-tuning, and generalized minimization of radiation in undesired directions as featured in equation (17). Furthermore, nulling performance with changes in the number of collaborating nodes and cluster radius is analyzed. Performance measures utilized include achieved null depth, width, nulling accuracy, and the resultant capacity at unintended receivers in nulling directions.

3.1. Performance Analysis against a Basic Null Steering Beamformer.

The performance of the developed null steering beamformer as per equation (17) is compared against that of the basic null steering beamformer depicted in equation (20). Typical research entailing basic null steering can be found in [8, 10, 12, 21].

$$\text{minimize: } f(\mathbf{W}) = -g_a \left| AF_{\phi_0,\theta_0}(\mathbf{W}) \right|^2$$
$$+ g_b \frac{1}{N} \sum_{n=1}^{N} \left| AF_{\phi_n,\theta_n}(\mathbf{W}) \right|^2, \quad (20)$$

where $g_a = 0.3$ and $g_b = 0.7$ are carefully selected constants intended to balance out a beam and null steering, $|AF_{\phi_0,\theta_0}(\mathbf{W})|$ is the magnitude of the array factor in the beam steering direction and $1/N \sum_{n=1}^{N} |AF_{\phi_n,\theta_n}(\mathbf{W})|$ is the average magnitude of the array factor in the null steering directions.

The utilized beam steering and null steering directions are as given in Table 4.

Typical radiation power patterns (in the form of mesh plots) obtained upon null steering using the schemes under study are as per Figures 5 and 6.

Typical radiation power patterns (in the form of contour plots) obtained upon null steering using the schemes under study are as per Figures 7 and 8.

A qualitative analysis of the radiation patterns presented in Figures 5–8 indicates the following:

(i) The proposed null steering scheme yields lower sidelobes

(ii) The proposed null steering scheme in general yields lower radiation in all undesired directions

(1) Step 1: initialize swarm particles (in a random manner).
(2) Step 2:
(a)   Evaluate the optimization function at all swarm particles.
(b)   Pick the optimal swarm particle as per the obtained optimization function values.
(3) Step 3: if the maximum number of iterations permitted has been exhausted, terminate the algorithm, else proceed to step 4.
(4) Step 4: if the count of iterations is half the specified maximum value, proceed to step 5, else proceed to step 7.
(5) Step 5: sort and rank swarm particles in accordance with their performance (as per the optimization function).
(6) Step 6: cull and randomly reinitialize swarm particles associated with poor performance.
(7) Step 7: update c_p, c_s, and w values (using a fuzzy logic-based look-up table).
(8) Step 8: update v_i and x_i. Revert to Step 2.

ALGORITHM 1: Culled-Fuzzy-Adaptive PSO Algorithm.
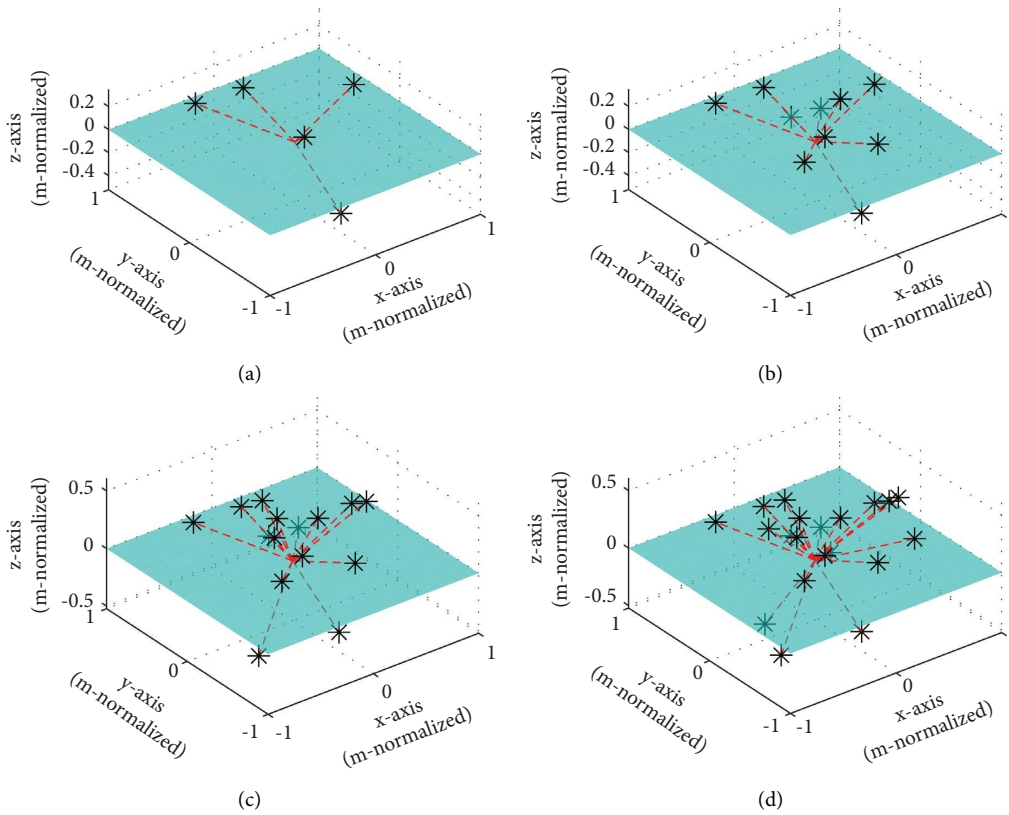

(a)

(b)

(c)

(d)

FIGURE 3: Collaborating nodes' positions 3 dimension configuration with varying node count: (a) 5 nodes; (b) 10 nodes; (c) 15 nodes; (d) 20 nodes.

TABLE 1: Collaborating nodes' positions 3 dimension configuration with varying node count: 5 and 10 nodes.

S. no.	10 nodes			5 nodes		
	Norm. rad. dist. (m)	El. angle (deg.)	Az. angle (deg.)	Norm. rad. dist. (m)	El. angle (deg.)	Az. angle (deg.)
1	0.4	61	−27	0.7	14	14
2	0.7	14	14	0.8	25	144
3	0.5	10	−59	0.6	26	99
4	0.8	25	144	0.5	34	−117
5	0.6	−9	72	0.7	−53	−63
6	0.8	−12	49			
7	0.6	26	99			
8	0.5	34	−117			
9	0.7	−53	−63			
10	0.6	16	−135			

TABLE 2: Collaborating nodes' positions 3 dimension configuration with varying node count: 15 and 20 nodes.

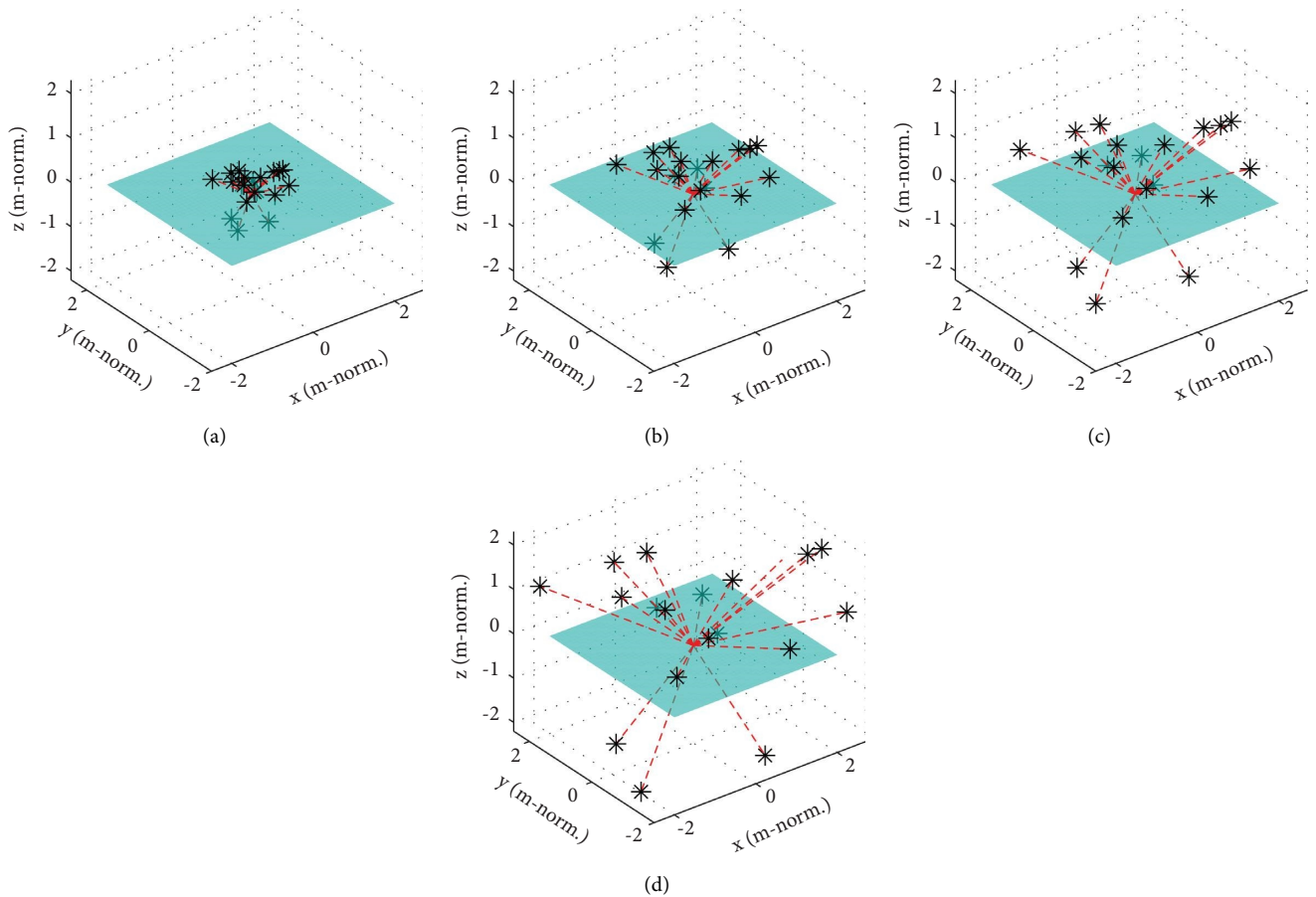| S. No.	20 nodes			15 nodes		
	Norm. rad. dist. (m)	El. angle (deg.)	Az. angle (deg.)	Norm. rad. dist. (m)	El. angle (deg.)	Az. angle (deg.)
1	0.4	61	−27	0.4	61	−27
2	0.7	14	14	0.7	14	14
3	0.5	10	−59	0.5	10	−59
4	0.5	58	108	0.5	58	108
5	0.8	25	144	0.8	25	144
6	0.8	43	−39	0.8	43	−39
7	0.3	56	180	0.3	56	180
8	0.6	−9	72	0.6	−9	72
9	0.8	−12	49	0.8	−12	49
10	0.7	54	−143	0.7	54	−143
11	0.4	24	117	0.6	26	99
12	0.6	26	99	0.5	34	−117
13	0.5	34	−117	0.7	−53	−63
14	0.8	13	−36	0.6	16	−135
15	0.8	40	−34	0.8	−42	−153
16	0.5	−22	37			
17	0.7	−22	−164			
18	0.7	−53	−63			
19	0.6	16	−135			
20	0.8	−42	−153			

(a)

(b)

(c)

(d)

FIGURE 4: 3-dimension cluster arrangements featuring cluster radii 1, 2, 3, and 4 (identical node distribution patterns have been utilized to allow for a fair comparison).

Table 3: Collaborating nodes' positions 3 dimension configuration with varying cluster radius.

S. no.	El. angle (deg.)	Az. angle (deg.)	Norm. rad. dist. (m)			
			1	2	3	4
1	61	−27	0.4	0.8	1.2	1.6
2	14	14	0.7	1.5	2.2	3.0
3	10	−59	0.5	1.0	1.5	2.1
4	58	108	0.5	1.0	1.5	2.1
5	25	144	0.8	1.6	2.5	3.3
6	43	−39	0.8	1.5	2.3	3.1
7	56	180	0.3	0.6	0.9	1.3
8	−9	72	0.6	1.1	1.7	2.2
9	−12	49	0.8	1.6	2.5	3.3
10	54	−143	0.7	1.5	2.2	3.0
11	24	117	0.4	0.9	1.3	1.7
12	26	99	0.6	1.2	1.8	2.4
13	34	−117	0.5	0.9	1.4	1.9
14	13	−36	0.8	1.5	2.3	3.1
15	40	−34	0.8	1.6	2.4	3.3
16	−22	37	0.5	0.9	1.4	1.9
17	−22	−164	0.7	1.4	2.1	2.7
18	−53	−63	0.7	1.3	2.0	2.6
19	16	−135	0.6	1.3	1.9	2.6
20	−42	−153	0.8	1.6	2.3	3.1

Table 4: Nulling and beam steering directions (in degrees). Notation: Az, azimuth; El, elevation; B.st., beam steering direction.

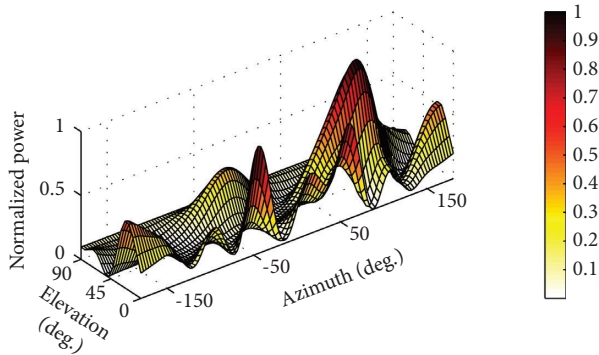|	Null 1	Null 2	Null 3	B. st.
Az	−100	0	150	80
El	40	40	40	40

Figure 5: Normalized power pattern: basic null steering.

Figure 9 comparatively depicts azimuth cut radiation power patterns corresponding to the null steering schemes under study. An outcome associated with conventional beam steering without nulling is also portrayed in the figure. A qualitative analysis of the azimuth cut radiation patterns indicate the following:

(i) The proposed null steering scheme yields wider nulls

(ii) The proposed null steering scheme yields a slightly narrower main lobe width

Table 5 gives the exact null depth values obtained using the proposed and basic null steering mechanisms. The
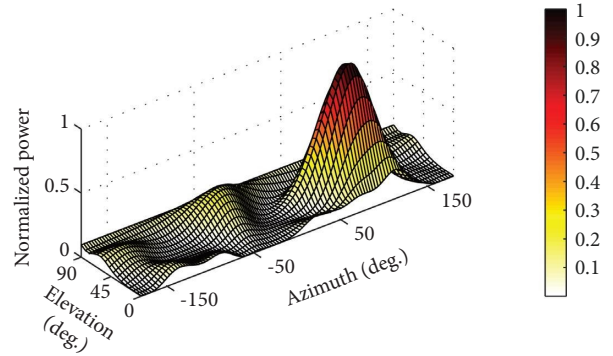

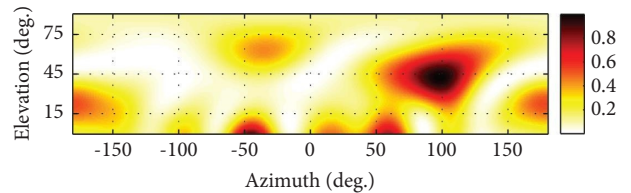Figure 6: Normalized power pattern: proposed null steering.

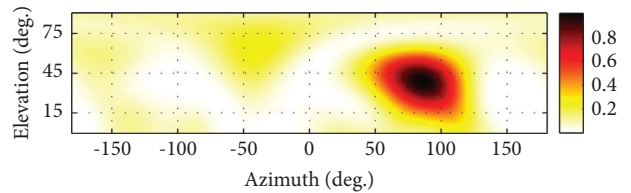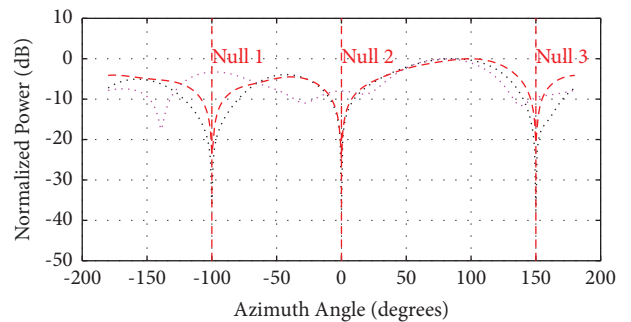Figure 7: Normalized power pattern: basic null steering.

Figure 8: Normalized power pattern: proposed null steering.

Figure 9: Azimuth cut of the normalized power pattern (at the elevation angle of 40 degrees) in a decibel scale.

proposed null steering approach yields deeper and low variance nulls (nearly identical depth values) in comparison to the basic null steering approach.

3.2. Performance Analysis with Change in the Number of Collaborating Nodes. In this section, 3-null placement is considered as per the listing given in Table 6.

TABLE 5: Null depth values (in dB) as obtained from the simulation results entailing the proposed and basic null steering mechanisms.

	Proposed null st.	Basic null st.	Conv. beamst.
Null 1	−36.67	−23.48	−3.29
Null 2	−37.73	−26.66	−7.99
Null 3	−37.59	−20.77	−9.66
Average	−37.33	−23.63	−6.98
Variance	0.22	5.78	7.28

TABLE 6: Nulling and beam steering directions (in degrees). Notation: Az, azimuth; El, elevation; B.st., beam steering direction.

	Null 1	Null 2	Null 3	B.st.
Az	−130	10	140	−60
El	60	60	60	60

Sets of 5, 10, 15, and 20 collaborating nodes are utilized in the null steering process.

Figure 10 comparatively illustrates the evolution of the nulling cost function (average outcome of 50 independent runs for the algorithms under study). It can be clearly deciphered that the 20-node configuration outperforms the other node configurations. Noteworthy, an increase in the number of collaborating nodes in a CB process might be associated with increased phase/time/frequency jitter at the nodes. This would inadvertently lead to unpredictable CB performance. It is expected that the performance superiority associated with an increase in collaborating nodes overcomes the performance downgrade associated with phase/time/frequency jitter at the collaborating nodes.

3.2.1. Beam Pattern Analysis

(1) Radiation Power Pattern. The azimuth cut of the resultant normalized radiation power pattern is as per Figure 11. The presented pattern is the average of 50 independent outcomes. It can be observed that an increase in the number of collaborating nodes yields slightly deeper and more accurate nulls. Beam steering performance is roughly identical.

(2) Null Depth Values. The obtained null depth values are given in Table 7. The values are the average outcomes of 50 independent runs. Analysis of variance test P-values are $5.0688E − 102$, $1.4277E − 132$, and $4.5124E − 166$ for null 1, 2, and 3, respectively. Going by the low P-values, the null depth values given in Table 7 bear statistically significant differences. The differences are captured/summarized in Table 8 following a Tukey–Kramer comparison test.

Table 9 presents null depth performance ranking (in accordance with the Tukey–Kramer comparison test results) upon using 20, 15, 10, and 5 nodes. A tie in rank in Table 9 implies statistically equivalent null depth values. Overall, the 20-node nulling procedure yields the best null depth performance.

Figure 12 comparatively illustrates the average normalized power observed in the nulling directions against the count of nodes. There is an exponential power decrease with an increase in the number of CB nodes.
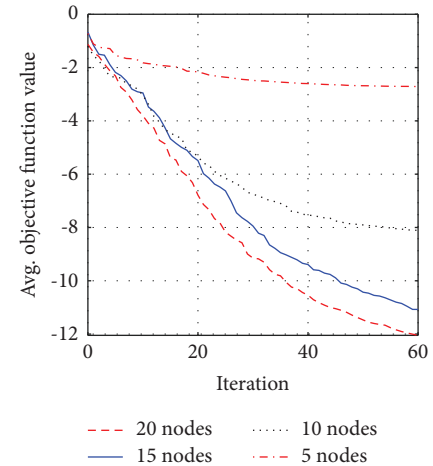

FIGURE 10: Average objective function value against algorithm iterations.
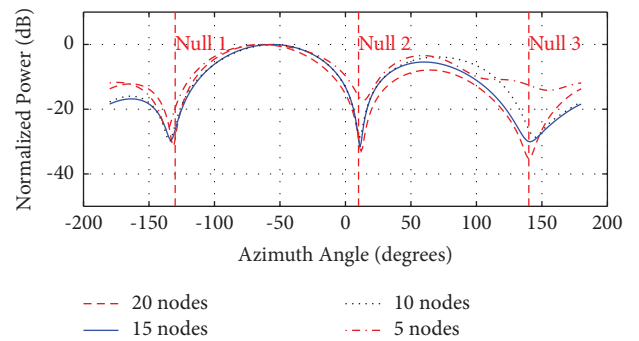

FIGURE 11: Azimuth cut of the normalized power pattern (at the elevation angle of 60 degrees) in a decibel scale.

TABLE 7: Null depth (in dB) corresponding to null steering using 20, 15, 10, and 5 nodes. SD denotes standard deviation.

	20 nodes		15 nodes		10 nodes		5 nodes	
	Depth	SD	Depth	SD	Depth	SD	Depth	SD
Null 1	−29.23	1.04	−26.42	1.08	−24.71	1.12	−19.61	1.21
Null 2	−28.92	1.13	−29.37	1.13	−27.70	1.25	−15.94	1.29
Null 3	−35.26	1.26	−29.98	1.07	−26.32	1.18	−12.56	1.33
Average	−31.14		−28.59		−26.24		−16.04	

TABLE 8: Tukey–Kramer comparison test. MD means different. MnD means not different.

Comparison	Null 1	Null 2	Null 3
20 vs. 15	MD	MnD	MD
20 vs. 10	MD	MD	MD
20 vs. 5	MD	MD	MD
15 vs. 10	MD	MD	MD
15 vs. 5	MD	MD	MD
10 vs. 5	MD	MD	MD

(3) Null Width Values. Null width values are given in Table 10. The values are measures corresponding to the azimuth-cut radiation pattern presented in Figure 11. There

TABLE 9: Null depth performance ranking corresponding to null steering using 20, 15, 10, and 5 nodes.

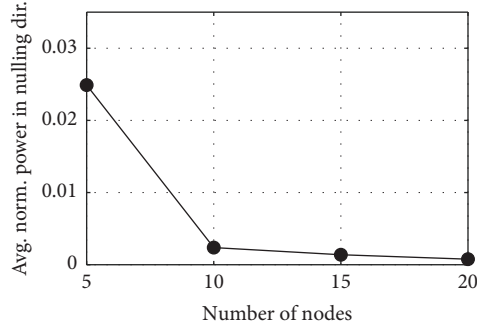|	Null 1	Null 2	Null 3	Total
20 nodes	1	1	1	3
15 nodes	2	1	2	5
10 nodes	3	3	3	9
5 nodes	4	4	4	12

FIGURE 12: Average normalized power in the nulling directions against the count of nodes.

TABLE 10: Null width (in degrees) corresponding to null steering using 20, 15, 10, and 5 nodes. The null width has been measured at the -20 dB power level in the average array factor.

	20	15	10	5
Null 1	14	20	19	13
Null 2	15	10	10	N/A
Null 3	41	50	37	N/A
Average	23.33	26.67	22.00	N/A

is no clear-cut trend in null width values for the 20, 15, and 10 nodes procedures. This can be attributed to

(i) Unpredictable relationship between the random collaborating nodes layout and null steering directions

(ii) The fact that the undertaken optimization process does not implicitly consider uniformity in the null width values

(4) Nulling Accuracy. Nulling accuracy values are given in Table 11. The 20 and 15 nodes nulling procedures yield higher nulling precision in comparison to the 10 and 5 nodes nulling.

(5) Power in the Desired and Undesired Directions. Normalized power values corresponding to the desired (beam steering) direction and all undesired directions are given in Table 12. The values are the average outcomes of 50 independent runs. There is a power performance mix cutting across node counts. For instance, moving from 15 to 10 nodes, there is an unexpected improvement in the power radiated towards the desired direction, but an expected increase in power radiated towards undesired directions. This can be attributed to the unpredictable relationship

TABLE 11: Nulling accuracy (in degrees) corresponding to null steering using 20, 15, 10, and 5 nodes.

	20	15	10	5
Null 1	1	3	4	6
Null 2	2	1	1	4
Null 3	0	1	5	15
Average	1.00	1.67	3.33	8.33

TABLE 12: Average power in the desired and all undesired directions corresponding to null steering using 20, 15, 10, and 5 nodes. SD denotes standard deviation.

No.		Desired dir.	Undesired dir.
20	Value	0.9528	0.1278
	SD	0.0007	0.0004
15	Value	0.9037	0.1214
	SD	0.0033	0.0001
10	Value	0.9357	0.1596
	SD	0.0050	0.0002
5	Value	0.6801	0.2281
	SD	0.0041	0.0001

between random node placement and the beam steering direction. A comprehensive performance comparison/trend is given in Table 13. Analysis of variance test P values are $8.4544E - 291$ and $0.0000E + 00$ for the power in the desired and undesired directions, respectively. Going by the low P values, the power values given in Table 12 bear statistically significant differences. The differences are captured/summarized in Table 14 following a Tukey–Kramer comparison test.

Table 13 presents the power performance ranking (in accordance with the Tukey–Kramer comparison test results) upon using 20, 15, 10, and 5 nodes. Overall, the 20-node nulling procedure yields the best power performance.

Figure 13 gives a comparative view of the average normalized power in the desired and undesired directions against the count of nodes.

3.2.2. Comparative Analysis of Communication Capacity at Unintended Receivers

(1) Capacity at Unintended Receivers Positioned in the Nulling Directions. Herein, communication capacity is evaluated at unintended receivers lying in the direction of the distinct 3 nulling points (as per the listing given in Table 6). This is done over a range of SNR values running from 0 to 40 dB.

Given an unintended receiver positioned at (-130 degrees azimuth, 60 degrees elevation), interference values are -29.23, -26.42, -24.71, and -19.61 for 20, 15, 10, and 5 nodes null steering, respectively. The resultant capacity is as per Figure 14. At a lower range of SNR values (0 to 10 dB), capacity performance is roughly identical for the four cases under comparison. At higher SNR values, 20 nodes of null steering offer distinctively better capacity performance. The best capacity improvement realized is 46 percent (at an SNR

TABLE 13: Power performance ranking corresponding to null steering using 20, 15, 10, and 5 nodes.

	Desired	Undesired	Total
20 nodes	1	2	3
15 nodes	3	1	4
10 nodes	2	3	5
5 nodes	4	4	8

TABLE 14: Tukey–Kramer comparison test. MD means different. MnD means not different.

Comparison	Desired	Undesired
20 vs. 15	MD	MD
20 vs. 10	MD	MD
20 vs. 5	MD	MD
15 vs. 10	MD	MD
15 vs. 5	MD	MD
10 vs. 5	MD	MD
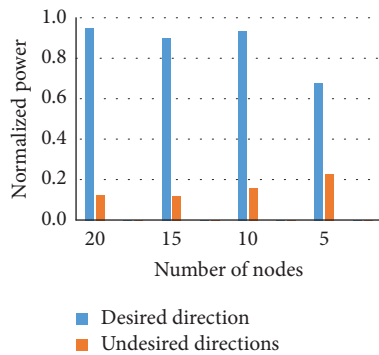
FIGURE 13: Average normalized power in the desired and undesired directions against the count of nodes (as per the data given in Table 12).

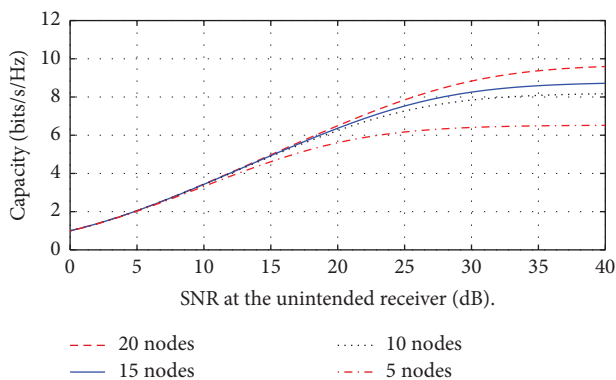FIGURE 14: Capacity comparison: unintended receiver at (−130 degrees azimuth, 60 degrees elevation).

FIGURE 15: Capacity comparison: unintended receiver at (10 degrees azimuth, 60 degrees elevation).

value of 40 dB); this is as evaluated with the capacity outcomes associated with 5 nodes and 20 nodes null steering.

Given an unintended receiver positioned at (10 degrees azimuth, 60 degrees elevation), interference values are −28.92, −29.37, −27.70, and −15.94 for 20, 15, 10, and 5 nodes null steering, respectively. The resultant capacity is as per Figure 15. At the lower range of SNR values (0 to 7.5 dB),
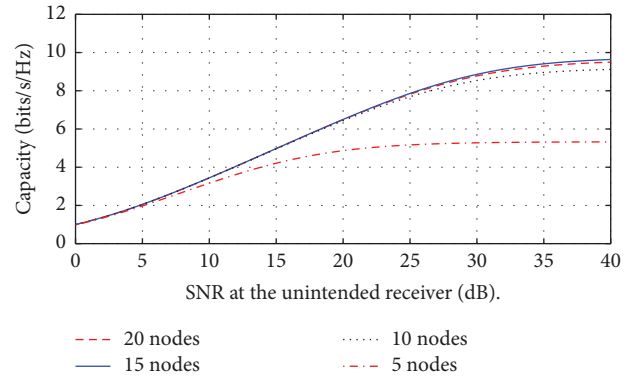
capacity performance is roughly identical for the four cases under comparison. At higher SNR values, 15, 20, and 10 nodes null steering offer better capacity performance. The best capacity improvement realized is 86 percent (at an SNR value of 40 dB); this is as evaluated with the capacity outcomes associated with 5 nodes and 15 nodes null steering.

Given an unintended receiver positioned at (140 degrees azimuth, 60 degrees elevation), interference values are −35.26, −29.98, −26.32, and −12.56 for 20, 15, 10, and 5 nodes null steering, respectively. The resultant capacity is as per Figure 16.

At the lower range of SNR values (0 to 5 dB), capacity performance is roughly identical for the four cases under comparison. Noise is dominant over interference hence the observed outcome. At higher SNR values, a higher node count offers better capacity performance. The best capacity improvement realized is 167 percent (at an SNR value of 40 dB); this is as evaluated with the capacity outcomes associated with 5 nodes and 20 nodes null steering. This capacity improvement value exceeds that reported in [6] (162 percent).

(2) Capacity at Unintended Receivers Distributed over Approx. All Directions Apart From the Beamsteering Direction. Herein, average communication capacity is evaluated over unintended receivers distributed over all azimuth and elevation directions (less the beam steering direction) at a one-degree precision. The resultant capacity is as per Figure 17. 20 and 15 nodes null steering offers better capacity performance. The best capacity improvement realized is 45 percent (at an SNR value of 40 dB); this is as evaluated with the capacity outcomes associated with 5 nodes and 20 nodes null steering.

3.3. Performance Analysis with Change in the Beamforming Cluster Radius. 3-null placement is considered as per the listing given in Table 15.

Wavelength-normalized CB cluster radius values of 1, 2, 3, and 4 are utilized in the null steering process.

Figure 18 comparatively illustrates the evolution of the nulling cost function (average outcome of 50 independent
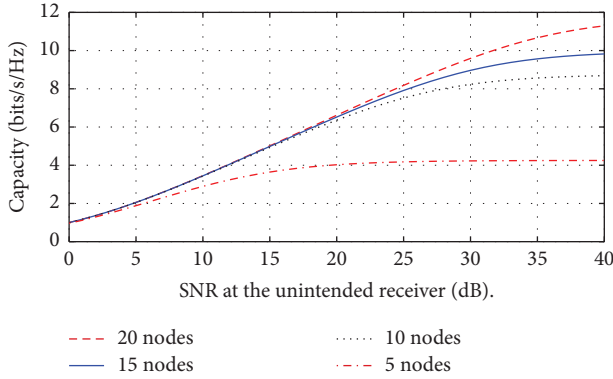
FIGURE 16: Capacity comparison: unintended receiver at (140 degrees azimuth, 60 degrees elevation).
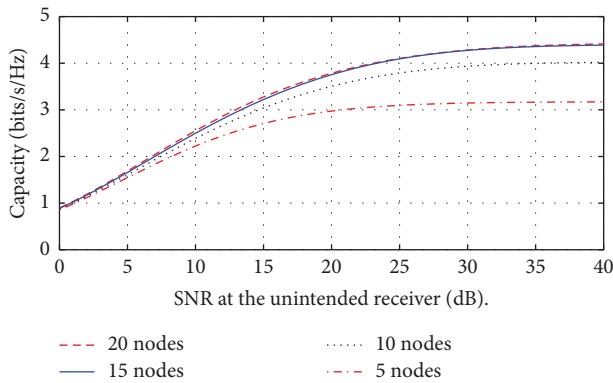

FIGURE 17: Capacity comparison: average outcome.

TABLE 15: Nulling and beam steering directions (in degrees). Notation: Az, azimuth; El, elevation; B.st., beam steering direction.

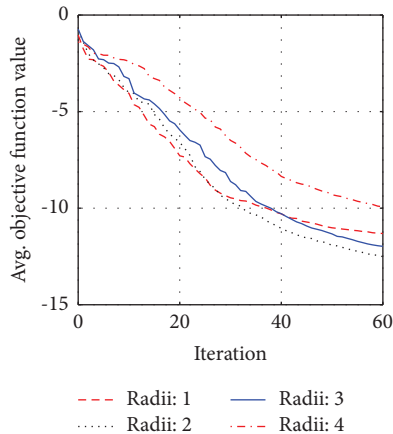|	Null 1	Null 2	Null 3	B.st.
Az	−135	30	110	−80
El	35	35	35	35

FIGURE 18: Average objective function value against algorithm iterations with variation in cluster radius. The radius values are wavelength-normalized.

runs for the algorithms under study). There is no clear-cut performance trend with changes in the CB cluster radius.

3.3.1. Beam Pattern Analysis

(1) Radiation Power Pattern. The azimuth cut of the resultant normalized radiation power pattern is as per Figure 19. The presented pattern is the average of 50 independent outcomes. An increase in cluster radius is associated with a decrease in null width and main beam width.

(2) Null Depth Values. Null depth values are given in Table 16. The values are the average outcomes of 50 independent runs. Analysis of variance test P values are $9.8641E − 88$, $9.2259E − 40$, and $3.6124E − 91$ for null 1, 2, and 3, respectively. Going by the low P values, the null depth values given in Table 16 are statistically different. The differences are captured/summarized in Table 17 following a Tukey–Kramer comparison test.

Table 18 presents null depth performance ranking (in accordance with the Tukey–Kramer comparison test results) upon using cluster radii 1, 2, 3, and 4. A tie in rank in Table 18 implies statistical equivalence. Overall, the radii 1 nulling procedure yields the best null depth performance. In general, there is no distinct relationship between cluster radius and null depth.

Figure 20 comparatively illustrates the average normalized power observed in the nulling directions against cluster radius. There is no clear-cut relationship between the power values and cluster radius.

(3) Null Width Values. Null width values are given in Table 19. The values are measures corresponding to the azimuth-cut radiation pattern presented in Figure 19. A large cluster radius is associated with narrow nulls.

(4) Nulling Accuracy. Nulling accuracy values are given in Table 20. Increase in cluster radius yields better nulling accuracy.

(5) Power in the Desired and Undesired Directions. Normalized power values corresponding to the desired direction and all undesired directions are given in Table 21. The values are the average outcomes of 50 independent runs. Analysis of variance test P values are $1.1228E − 197$ and $0.0000E + 00$ for the power in the desired and undesired directions, respectively. Going by the low P values, the power values given in Table 21 bear statistically significant differences. The differences are captured/summarized in Table 22 following a Tukey–Kramer comparison test.

Table 23 presents power performance ranking (in accordance with the Tukey–Kramer comparison test results) upon using cluster radii 1, 2, 3, and 4. A tie in rank in Table 23 implies statistical equivalence. Overall, as per Table 23, there is a power performance "mix." This can be attributed to the following facts:

 (i) At a small cluster radius, prominent outcomes are a wide main beam, wide nulls, and few low-leveled sidelobes

 (ii) At a large cluster radius, prominent outcomes are a narrow main beam, narrow nulls, and a number of average-leveled sidelobes
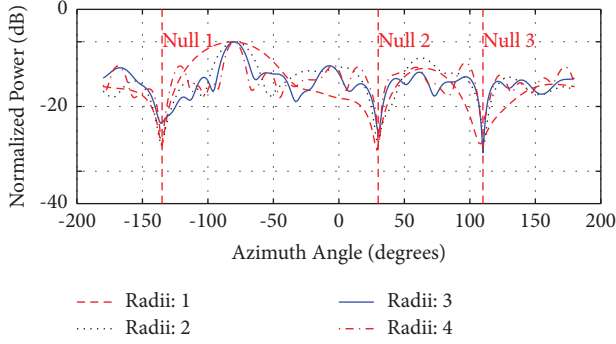
FIGURE 19: Azimuth cut of the normalized power pattern (at the elevation angle of 35 degrees) in a decibel scale. The radius values are wavelength-normalized.

FIGURE 20: Average normalized power in the nulling directions against cluster radius. The radius values are wavelength-normalized.

TABLE 16: Null depth (in dB) corresponding to null steering at radii 1, 2, 3, and 4 (wavelength-normalized). SD denotes standard deviation.

	Radii: 1		Radii: 2		Radii: 3		Radii: 4	
	Depth	SD	Depth	SD	Depth	SD	Depth	SD
Null 1	−32.07	1.04	−31.13	1.08	−25.02	1.12	−31.83	1.21
Null 2	−32.03	1.13	−31.47	1.13	−28.26	1.25	−31.44	1.29
Null 3	−30.48	1.26	−28.78	1.07	−34.37	1.18	−25.17	1.33
Average	−31.53		−30.46		−29.22		−29.48	

TABLE 17: Tukey–Kramer comparison test. MD means different. MnD means not different.

Comparison	Null 1	Null 2	Null 3
Radii 1 vs. Radii 2	MD	MnD	MD
Radii 1 vs. Radii 3	MD	MD	MD
Radii 1 vs. Radii 4	MnD	MnD	MD
Radii 2 vs. Radii 3	MD	MD	MD
Radii 2 vs. Radii 4	MD	MnD	MD
Radii 3 vs. Radii 4	MD	MD	MD

TABLE 18: Null depth performance ranking corresponding to null steering using cluster radii 1, 2, 3, and 4 (wavelength normalized).

	Null 1	Null 2	Null 3	Total
Radii: 1	1	1	2	4
Radii: 2	3	1	3	7
Radii: 3	4	4	1	9
Radii: 4	1	1	4	6

Figure 21 gives a comparative view of the average normalized power in the desired and undesired directions against cluster radius.

3.3.2. Comparative Analysis of Communication Capacity at Unintended Receivers

(1) Capacity at Unintended Receivers Positioned in the Nulling Directions. Herein, communication capacity is evaluated at unintended receivers lying in the direction of the distinct 3 nulling points (as per the listing given in
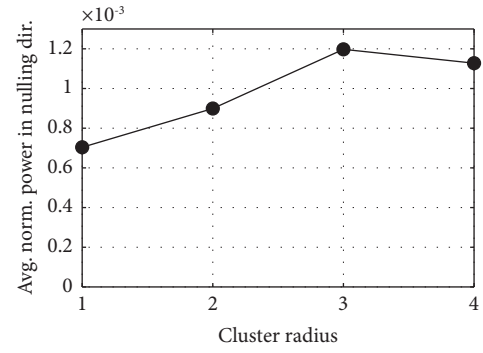
TABLE 19: Null width (in degrees) corresponding to null steering at radii 1, 2, 3, and 4 (wavelength normalized). The null width has been measured at the −20 dB power level in the average array factor.

	1	2	3	4
Null 1	14	15	15	8
Null 2	20	16	7	5
Null 3	31	8	6	7
Average	21.67	13.00	9.33	6.67

TABLE 20: Nulling accuracy (in degrees) corresponding to null steering at wavelength normalized radii 1, 2, 3, and 4 (as per the average array factor).

	Rad 1	Rad 2	Rad 3	Rad 4
Null 1	0	1	1	0
Null 2	1	0	0	0
Null 3	2	1	0	1
Average	1.00	0.67	0.33	0.33

TABLE 21: Average power in the desired and all undesired directions corresponding to null steering at cluster radii 1, 2, 3, and 4 (wavelength normalized). SD denotes standard deviation.

Rad.		Desired dir.	Undesired dir.
1	Value	0.984171708	0.095203404
	SD	0.000360835	0.000113346
2	Value	0.961331761	0.066133465
	SD	0.001395834	$6.14076E-05$
3	Value	0.978670252	0.069050449
	SD	0.000666423	0.00027976
4	Value	0.976489929	0.089864776
	SD	0.000542081	0.000200544

TABLE 22: Tukey–Kramer comparison test. MD means different. MnD means not different.

Comparison	Desired	Undesired
Radii 1 vs. radii 2	MD	MD
Radii 1 vs. radii 3	MD	MD
Radii 1 vs. radii 4	MD	MD
Radii 2 vs. radii 3	MD	MD
Radii 2 vs. radii 4	MD	MD
Radii 3 vs. radii 4	MD	MD

TABLE 23: Power performance ranking corresponding to null steering at radii 1, 2, 3, and 4 (wavelength normalized).

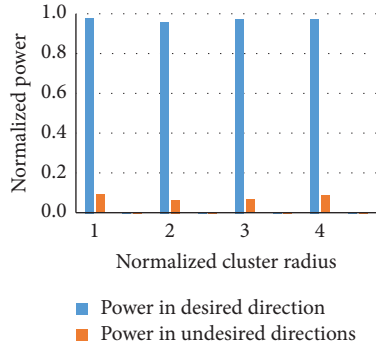|	Des	Undes	Total
Radii: 1	1	4	5
Radii: 2	4	1	5
Radii: 3	2	2	4
Radii: 4	3	3	6

FIGURE 21: Average normalized power in the desired and undesired directions against cluster radius (wavelength normalized).

FIGURE 22: Capacity comparison: unintended receiver at (−135 degrees azimuth, 35 degrees elevation). The radius values are wavelength normalized.

FIGURE 23: Capacity comparison: unintended receiver at (30 degrees azimuth, 35 degrees elevation). The radius values are wavelength normalized.

FIGURE 24: Capacity comparison: unintended receiver at (110 degrees azimuth, 35 degrees elevation). The radius values are wavelength normalized.

Table 15). This is done over a range of SNR values running from 0 to 40 dB.

Given an unintended receiver positioned at (−135 degrees azimuth, 35 degrees elevation), average interference values are −32.07, −31.13, −25.02, and −31.83 for 1, 2, 3, and 4 cluster radius configurations, respectively. The resultant capacity is as per Figure 22. At the lower range of SNR values (0 to 15 dB), capacity performance is roughly identical for the four cases under comparison. At higher SNR values, the 3-cluster radius configuration offers better capacity performance. The best capacity improvement realized is 25 percent (at an SNR value of 40 dB); this is as evaluated with the capacity outcomes associated with cluster radii 1 and cluster radii 3 null steerings.

Given an unintended receiver positioned at (30 degrees azimuth, 35 degrees elevation), average interference values are −32.03, −31.47, −28.26, and −31.44 for 1, 2, 3, and 4 cluster radius configurations respectively. The resultant capacity is as per Figure 23. At the lower range of SNR values (0 to 20 dB), capacity performance is roughly identical for the four cases under comparison. At higher SNR values, 1, 2, and 4 cluster radius configurations offer roughly identical capacity performance. The best capacity improvement realized is 11 percent (at an SNR value of 40 dB); this is as evaluated with the capacity outcomes associated with cluster radii 1 and cluster radii 3 null steerings.

Given an unintended receiver positioned at (110 degrees azimuth, 35 degrees elevation), average interference values are −30.48, −28.78, −34.37, and −25.17 for 1, 2, 3, and 4 cluster radius configurations respectively. The resultant capacity is as per Figure 24. At the lower range of SNR values (0 to 15 dB), capacity performance is roughly identical for the four cases under comparison. The best capacity improvement realized is 35 percent (at an SNR value of 40 dB);
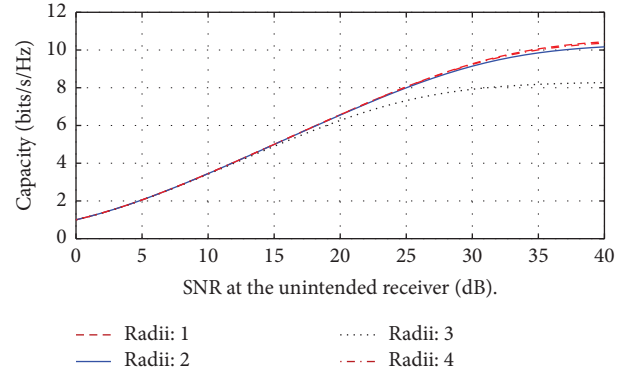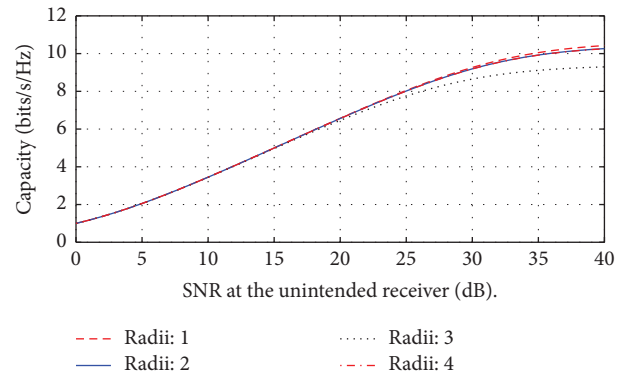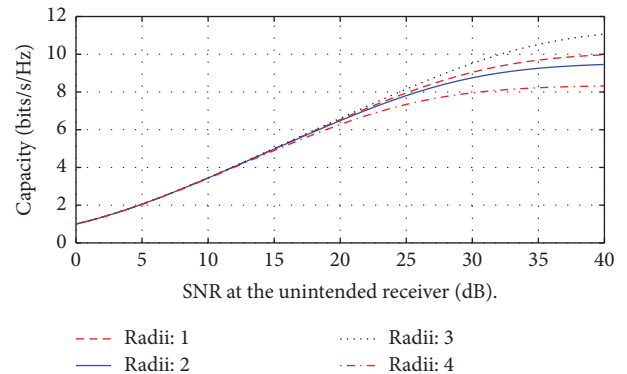
this is as evaluated with the capacity outcomes associated with cluster radii 3 and cluster radii 4 null steerings.

(2) Capacity at Unintended Receivers Distributed Over Approx. All Directions apart from the Beam steering Direction. Herein, average communication capacity is evaluated
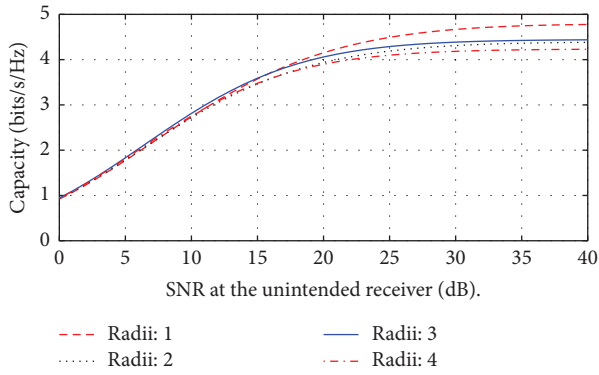
Figure 25: Capacity comparison: average outcome. The radius values are wavelength normalized.

over unintended receivers distributed over all azimuth and elevation directions (less the beam steering direction) at a one-degree precision. The resultant capacity is as per Figure 25. The cluster radius 1 configuration offers slightly better capacity performance. The best capacity improvement realized is 12 percent (at an SNR value of 40 dB); this is as evaluated with the capacity outcomes associated with cluster radii 1 and cluster radii 4 null steerings.

4. Conclusion

This paper has presented a nulling procedure aimed at reducing interference at unintended receivers upon CB in WSNs. A multiobjective criterion has been developed with the considerations listed as follows:

(i) Beam steering.

(ii) Deep and wide nulling.

(iii) Minimizing radiation power in all directions outside of the intended sink direction.

(iv) Simultaneous optimization of node transmit amplitude and phase to achieve the aforementioned items. In current literature, nulling is performed through phase weighting after a conventional beam steering procedure.

(v) 3-dimension WSN node layout.

The performance of the developed (improved) null steering beamformer has been validated through a comparison with a basic null steering procedure yielding the following outcomes:

(i) Lower sidelobes

(ii) Lower radiation in all undesired directions

(iii) Wider nulls

(iv) Slightly narrower main lobe width

The above positive outcomes listed above can be attributed to

(i) Introduction of a worthwhile undesired radiation suppression mechanism as per equation (14)

(ii) Introduction of a mechanism aimed at null widening as per equation (16)

Furthermore, performance analysis has been carried out with the considerations listed as follows:

(i) Performance analysis with change in the number of collaborating nodes

(ii) Performance analysis with change in beamforming cluster radius

Performance measures utilized include null depth, null width, and nulling accuracy. It has been established that an increase in the number of collaborating nodes leads to deeper nulls, a marginal decrease in null width, and increased nulling accuracy. A higher number of collaborating nodes has the advantage of distributing radiation power across more nodes. On the negative side, there is an increase in intra-CB cluster communication. Moreover, an increase in the number of collaborating nodes in a CB process might be associated with increased phase, time, and frequency jitter at the collaborating nodes. This would inadvertently lead to unpredictable CB performance. It is expected that the advantages associated with an increase in the number of collaborating nodes overcome performance downgrade associated with phase, time, and frequency jitter at the collaborating nodes. An increase in CB cluster radius leads to slightly deeper nulls at the expense of null width. Increased cluster radius is disadvantageous in terms of an increase in transmission energy usage at collaborating nodes when performing intracluster communication. A node count/ cluster radius balance should be struck to yield an optimal null steering outcome. Deep nulls directly imply reduced interference at unintended receivers. Wide nulls reduce CB frequency in cases of mobile unintended receivers and reduce interference in other distinct CB clusters (collaborating nodes are bound to be spatially distributed). Nulling is associated with a reduction in interference/capacity improvement at unintended receivers. The best capacity improvement realized is 167 percent (at an SNR value of 40 dB); this is as evaluated with the capacity outcomes associated with 5 nodes and 20 nodes null steering. This capacity improvement value exceeds that reported in [6] (162 percent).

5. Limitations and Future Work

The research work presented herein assumes that there is no "expiry" or failure of sensor nodes participating in the CB process. Sensor nodes are failure-prone owing to energy exhaustion. A potential area of future research would entail working on CB imperfectness upon failure of a collaborating node. In this research work, it has been assumed that there is no phase/time/frequency jitter at the collaborating nodes. Phase/time/frequency jitter would inadvertently lead to unpredictable CB performance. It is essential to analyze CB performance with phase/time/frequency jitter at the collaborating nodes. As per the observed research outcomes, beam pattern nulls lacked uniformity in null widths. It is

crucial to develop a scheme that ascertains null width uniformity when executing multiple nulling procedures.

Abbreviations

APSO:	Accelerated particle swarm optimization
BA:	Bat algorithm
CB:	Collaborative beamforming
CORPS:	Coherently radiating periodic structure
FA:	Firefly algorithm
FBS:	Fibonacci branch search
GA:	Genetic algorithm
IoT:	Internet of things
IWO:	Invasive weed optimization
MANET:	Mobile ad hoc network
MVDR:	Minimum variance distortionless response
PSO:	Particle swarm optimization
SNR:	Signal-to-noise ratio
ULA:	Uniform linear array
WSN:	Wireless sensor network
$A(\mathbf{r}, t)$:	Magnetic potential at location $\mathbf{r}$, time t
$\mathbf{J}$:	Current density
C:	Wave velocity
$\mathbf{F}(\mathbf{k})$:	Radiation vector at wave number $\mathbf{k}$
AF:	Array factor
$\mathbf{R}_t$:	Position vector of tth node
MAF:	Mean array factor
ϕ:	Azimuthal direction
θ:	Elevation direction
$\mathbf{W}$:	Node transmit weight.

Data Availability

The data used to support the findings of this study are available from the corresponding author upon request.

Conflicts of Interest

The authors declare that they have no conflicts of interest.

Acknowledgments

References

[1] S. Felici-Castell, E. A. Navarro, J. J. Pérez-Solano, J. Segura-García, and M. García-Pineda, "Practical considerations in the implementation of collaborative beamforming on wireless sensor networks," *Sensors*, vol. 17, no. 2, p. 237, 2017.

[2] S. Liang, Z. Fang, G. Sun et al., "A joint optimization approach for distributed collaborative beamforming in mobile wireless sensor networks," *Ad Hoc Networks*, vol. 106, Article ID 102216, 2020.

[3] E. A. Navarro-Camba, S. Felici-Castell, J. Segura-García, M. García-Pineda, and J. J. Pérez-Solano, "Feasibility of a stochastic collaborative beamforming for long range communications in wireless sensor networks," *Electronics*, vol. 7, no. 12, p. 417, 2018.

[4] M. Z. Hasan and H. Al-Rizzo, "Beamforming optimization in internet of things applications using robust swarm algorithm in conjunction with connectable and collaborative sensors," *Sensors*, vol. 20, no. 7, p. 2048, 2020.

[5] G. Sun, Y. Liu, Z. Chen et al., "Energy efficient collaborative beamforming for reducing sidelobe in wireless sensor networks," *IEEE Transactions on Mobile Computing*, vol. 20, 2019.

[6] S. Jayaprakasam, S. K. Abdul Rahim, C. Y. Leow, and T. O. Ting, "Sidelobe reduction and capacity improvement of open-loop collaborative beamforming in wireless sensor networks," *PLoS One*, vol. 12, no. 5, Article ID e0175510, 2017.

[7] G. Sun, X. Zhao, S. Liang, Y. Liu, Y. Zhang, and V. C. Leung, "A hybrid optimization approach for suppressing sidelobe level and reducing transmission power in collaborative beamforming," in *Proceedings of the 2019 IEEE 90th Vehicular Technology Conference (VTC2019-Fall)*, pp. 1–6, IEEE, Honolulu, HI, USA, September 2019.

[8] T. Van Luyen and T. V. B. Giang, "Null-steering beamformer using bat algorithm," *Applied Computational Electromagnetics Society Journal*, vol. 33, no. 1, 2018.

[9] B. Babakhani and S. K. Sharma, "Dual null steering and limited beam peak steering using triple-mode circular microstrip patch antenna," *IEEE Transactions on Antennas and Propagation*, vol. 65, no. 8, pp. 3838–3848, 2017.

[10] Z.-K. Zhang, L.-J. Sun, and L. Xu, "Multiple beamforming with null steering based on improved invasive weed optimization," in *Proceedings of the 2020 12th International Conference on Knowledge and Smart Technology (KST)*, pp. 36–40, IEEE, Pattaya, Thailand, January 2020.

[11] N. Saliani, M. Bemani, and H. Kazemi, "Modified corps beamforming network with null-steering capability," *IET Microwaves, Antennas & Propagation*, vol. 13, no. 8, pp. 1208–1213, 2019.

[12] S. N. Shahab, B. S. Sumait, M. K. Awsaj, and N. H. Noordin, "Null steering optimization based mvdr beamformer using firefly algorithm for adaptive beamforming application," *Solid State Technology*, vol. 63, no. 6, pp. 9344–9359, 2020.

[13] Y. Jiang, G. Tong, H. Yin, and N. Xiong, "A pedestrian detection method based on genetic algorithm for optimize xgboost training parameters," *IEEE Access*, vol. 7, pp. 118310–118321, 2019.

[14] V. Palazzi, F. Alimenti, L. Roselli, and P. Mezzanotte, "Beamforming approach for steerable null synthesis in a four-element conformal array fed with a radio-frequency reconfigurable network," in *Proceedings of the 2021 XXXIVth General Assembly and Scientific Symposium of the International Union of Radio Science (URSI GASS)*, pp. 1–4, IEEE, Rome, Italy, August 2021.

[15] J. Kong, F. T. Dagefu, and B. M. Sadler, "Multi-group distributed nullforming and sectorized jamming," *IEEE Transactions on Vehicular Technology*, vol. 70, no. 9, pp. 9572–9576, 2021.

[16] L. Lan, G. Liao, J. Xu, Y. Zhang, and B. Liao, "Transceive beamforming with accurate nulling in fda-mimo radar for imaging," *IEEE Transactions on Geoscience and Remote Sensing*, vol. 58, no. 6, pp. 4145–4159, 2020.

[17] K. Buchanan, J. Jensen, C. Flores-Molina, S. Wheeland, and G. H. Huff, "Null beamsteering using distributed arrays and shared aperture distributions," *IEEE Transactions on Antennas and Propagation*, vol. 68, no. 7, pp. 5353–5364, 2020.

[18] M. V. Lipski, S. Kompella, and R. M. Narayanan, "Exploring transmit null forming in open-loop coherent distributed arrays," in *Radar Sensor Technology XXIV*, vol. 11408, pp. 172–181, SPIE, 2020.

[19] H. Zhang and F. Zeng, "Implementation of a novel fibonacci branch search optimizer for the design of the low sidelobe and deep nulling adaptive beamformer," *International Journal of Microwave and Wireless Technologies*, vol. 12, no. 7, pp. 660–677, 2020.

[20] H. Jung and I.-H. Lee, "Distributed null-steering beamformer design for physical layer security enhancement in internet-of-things networks," *IEEE Systems Journal*, vol. 15, no. 1, pp. 277–288, 2021.

[21] N. N. N. Abd Malik, M. Esa, S. Yusof, and N. A. Latiff, "Collaborative beamforming null-steering array for wireless sensor networks," in *Proceedings of the 2014 IEEE 2nd International Symposium on Telecommunication Technologies (ISTT)*, pp. 316–320, IEEE, Langkawi, Malaysia, November 2014.

[22] J. Li, H. Kang, G. Sun, S. Liang, Y. Liu, and Y. Zhang, "Physical layer secure communications based on collaborative beamforming for uav networks: a multi-objective optimization approach," in *Proceedings of the IEEE INFOCOM 2021-IEEE Conference on Computer Communications*, pp. 1–10, IEEE, Vancouver, BC, Canada, May 2021.

[23] J. Xu, Y. Yang, Y. Yang, L. Zhang, J. Wang, and J. Zhuang, "Two-step phase synchronization algorithm for distributed collaborative beamforming," in *Proceedings of the 2021 IEEE 6th International Conference on Signal and Image Processing (ICSIP)*, pp. 1188–1192, IEEE, Nanjing, China, October 2021.

[24] J. R. Mohammed, "Performance optimization of the arbitrary arrays with randomly distributed elements for wireless sensor networks," *Journal of Telecommunication, Electronic and Computer Engineering*, vol. 11, no. 4, pp. 63–68, 2019.

[25] O. Smida, S. Zaidi, S. Affes, and S. Valaee, "Robust distributed collaborative beamforming for wireless sensor networks with channel estimation impairments," *Sensors*, vol. 19, no. 5, p. 1061, 2019.

[26] C. O. Nnamani, M. R. Khandaker, and M. Sellathurai, "Joint beamforming and location optimization for secure data collection in wireless sensor networks with uav-carried intelligent reflecting surface," 2021, https://arxiv.org/abs/2101.06565.

[27] J. Liu, C.-H. R. Lin, Y.-C. Hu, and P. K. Donta, "Joint beamforming, power allocation, and splitting control for swipt-enabled iot networks with deep reinforcement learning and game theory," *Sensors*, vol. 22, no. 6, p. 2328, 2022.

[28] W. Guo, N. Xiong, H.-C. Chao, S. Hussain, and G. Chen, "Design and analysis of self-adapted task scheduling strategies in wireless sensor networks," *Sensors*, vol. 11, no. 7, pp. 6533–6554, 2011.

[29] X. Wang, Q. Li, N. Xiong, and Y. Pan, "Ant colony optimization-based location-aware routing for wireless sensor networks," in *International Conference on Wireless Algorithms, Systems, and Applications*, pp. 109–120, Springer, Cham, 2008.

[30] A. Khare, R. Gupta, and P. K. Shukla, "Improving the protection of wireless sensor network using a black hole optimization algorithm (bhoa) on best feasible node capture attack," in *IoT and Analytics for Sensor Networks*, pp. 333–343, Springer, Cham, 2022.

[31] R. K. Yadav and R. P. Mahapatra, "Hybrid metaheuristic algorithm for optimal cluster head selection in wireless sensor network," *Pervasive and Mobile Computing*, vol. 79, Article ID 101504, 2022.

[32] N. Yuvaraj, R. A. Raja, T. Karthikeyan, and K. Praghash, "Improved authentication in secured multicast wireless sensor network (mwsn) using opposition frog leaping algorithm to resist man-in-middle attack," *Wireless Personal Communications*, vol. 123, no. 2, pp. 1715–1731, 2022.

[33] R. Natarajan, G. Megharaj, A. Marchewka, P. B. Divakarachari, and M. R. Hans, "Energy and distance based multi-objective red fox optimization algorithm in wireless sensor network," *Sensors*, vol. 22, no. 10, p. 3761, 2022.

[34] F. Xia, R. Hao, J. Li, N. Xiong, L. T. Yang, and Y. Zhang, "Adaptive gts allocation in ieee 802.15.4 for real-time wireless sensor networks," *Journal of Systems Architecture*, vol. 59, no. 10, pp. 1231–1242, 2013.

[35] P. Kumar, R. Kumar, G. Srivastava et al., "Ppsf: a privacy-preserving and secure framework using blockchain-based machine-learning for iot-driven smart cities," *IEEE Transactions on Network Science and Engineering*, vol. 8, no. 3, pp. 2326–2341, 2021.

[36] C. Wu, C. Luo, N. Xiong, W. Zhang, and T.-H. Kim, "A greedy deep learning method for medical disease analysis," *IEEE Access*, vol. 6, pp. 20021–20030, 2018.

[37] M. D. Ramos, A. D. Foster, S. F. Castell, V. G. Fos, and J. J. P. Solano, "Gatherer: an environmental monitoring application based on ipv6 using wireless sensor networks," *International Journal of Ad Hoc and Ubiquitous Computing*, vol. 13, no. 3/4, pp. 209–217, 2013.

[38] Q. Zhang, *Environment pollution analysis on smart cities using wireless sensor networks*, Strategic Planning for Energy and the Environment, 2022.

[39] M. A. Kafi, Y. Challal, D. Djenouri, M. Doudou, A. Bouabdallah, and N. Badache, "A study of wireless sensor networks for urban traffic monitoring: applications and architectures," *Procedia Computer Science*, vol. 19, pp. 617–626, 2013.

[40] Z. Sheng, C. Mahapatra, C. Zhu, and V. C. M. Leung, "Recent advances in industrial wireless sensor networks toward efficient management in iot," *IEEE Access*, vol. 3, pp. 622–637, 2015.

[41] S. Rani, V. Sai, and R. Maheswar, *Iot and Wsn Based Smart Cities: A Machine Learning Perspective*.

[42] A. Gohari, A. B. Ahmad, R. B. A. Rahim, A. Supa'at, S. Abd Razak, and M. S. M. Gismalla, "Involvement of surveillance drones in smart cities: a systematic review," *IEEE Access*, vol. 10, 2022.

[43] B. Sahu, A. Panigrahi, and S. N. Mohanty, "Health monitoring system for cancer care using iot," in *Real-Life Applications of the Internet of Things*, pp. 203–229, Apple Academic Press, 2022.

[44] C. Su and W. Chen, "Design of remote real-time monitoring and control management system for smart home equipment based on wireless multihop sensor network," *Journal of Sensors*, vol. 2022, pp. 1–10, 2022.

[45] J. Arshad, A. U. Rehman, M. T. B. Othman et al., "Deployment of wireless sensor network and iot platform to implement an intelligent animal monitoring system," *Sustainability*, vol. 14, no. 10, p. 6249, 2022.

[46] M. Ghosh and Y. Shacham-Diamand, "Green energy-based efficient iot sensor network for small farms," in *Electrical and Computer Engineering: First International Congress, ICECENG 2022, Virtual Event*, vol. 436, p. 15, Springer Nature, 2022.

[47] S. J. Orfanidis, *Electromagnetic Waves and Antennas*, Rutgers University, 2016.

[48] R. M. Maina, P. Kibet Lang'at, and P. K. Kihato, "Collaborative beamforming in wireless sensor networks using a novel

particle swarm optimization algorithm variant," *Heliyon*, vol. 7, no. 10, Article ID e08247, 2021.

[49] T. Weise, *Global Optimization Algorithms: Theory and Applications*, Kassel: University of Kassel, 2009.

[50] Maurice-Clerc, *Particle Swarm Optimization*, ISTE Ltd, London, UK, 2006.

[51] P. Erdogmus, *Particle Swarm Optimization with Applications*, InTechOpen, 2018.

[52] R. Eberhart and Y. Shi, "Comparing inertia weights and constriction factors in particle swarm optimization," *Proceedings of the IEEE congress on evolutionary computation*, pp. 84–88, La Jolla, CA, USA, July 2000.

[53] J. Kennedy and R. Eberhart, "Particle swarm optimization," in *Proceedings of the IEEE International Conference on Neural Networks*, pp. 1942–1948, Perth, WA, Australia, November 1995.

[54] S. M. Ross, *Introduction to Probability and Statistics for Engineers and Scientists*, Elsevier, 2014.

[55] J. Frost, *Central Limit Theorem Explained*, Online, June 2021.

[56] L. M. Connelly, "Introduction to analysis of variance (anova)," *Medsurg Nursing*, vol. 30, no. 3, pp. 218–158, 2021.

[57] S. Lee and D. K. Lee, "What is the proper way to apply the multiple comparison test?" *Korean Journal of Anesthesiology*, vol. 73, no. 6, p. 572, 2020.